Investigation of shock-induced flow separation over a transonic compressor blade by conditionally averaged PIV and high-speed shadowgraphs

J. Klinner[1,*], A. Hergt[1], S. Grund[1], and C. Willert[1]
[1] German Aerospace Center (DLR), Institute of Propulsion Technology, Köln, Germany
[*] Corresponding author: joachim.klinner@dlr.de

Keywords: shock-induced separation, bubble separation, conditional average, PIV, transonic buffeting, transition control, SBLI

ABSTRACT

The impact of separation control has been investigated in a highly loaded transonic compressor cascade at an inlet Mach number of 1.21 and a chord based Reynolds number of 1.4×10^6. Applied control devices are air jet vortex generators (AJVG) and a surface roughness patch. Comparative flows without transition control imply a variation of the upstream turbulence level from 0.5% to 2.5%. Above the suction side, velocities of the unsteady separation region have been captured by particle image velocimetry (PIV). The aerodynamic load alternation due to shock motion results in flexure of the blade surface which have been measured and compensated prior to PIV processing. Single PIV shots indicate shape variations of both the lambda shock system and the associated separation region while the shock foot position is fluctuating within a range of up to 23% of chord. Large sets of statistically independent PIV samples are conditionally averaged upon instantaneous passage shock positions at a resolution of 1% of chord length to quantify the size of flow separation. Large bubble separation occurs if the turbulence of the incoming flow is low. The separation region becomes smaller when AJVGs are applied but still exhibits bubble separation at rear shock positions. The size of the separation region is significantly reduced either if a roughness patch is applied or if the turbulence level of the incoming flow is high. The frequency range of shock motion is analyzed by shock tracking on the basis of high speed shadowgraphs. A Fourier analysis of shock motion in the low frequency range (<1khz) indicates the highest spectral densities for the turbulent case and the lowest densities if roughness patch are applied. Joined probability density distributions of blade displacements and amplitudes of shock movement revealed that upward transverse blade deflections are more frequent at shock positions downstream of the mean shock position while downward deflections are more frequent at frontal shock positions.

1. Introduction

When designing transonic blades for aero engine fans or axial compressors, the correct estimation of the of phenomenon of shock wave boundary layer interaction (SBLI) is of crucial importance. The transient behavior of the interaction is often coupled with a large amplitude movement of normal or near normal shocks at low frequencies, which is highly undesirable due to the unsteady pressure fluctuations on the blade, as it leads to additional unsteady aerodynamic loads [4, 6]. Especially low frequency motion of the normal shock is accompanied by low frequency pressure fluctuations [2] on the blade surface which in turn can reduce the buffet boundary or even increase the strength of blade vibrations [12, 6]. As a consequence machine maintenance cycles are shortened and possibly the machine fatigue life is reduced. Another important point is that SBLI can cause shock-induced flow separation which additionally enhances the viscous losses of the compressor blading by enhancing dissipation in the boundary layer [3]. The formation of large scale eddies in the separation region

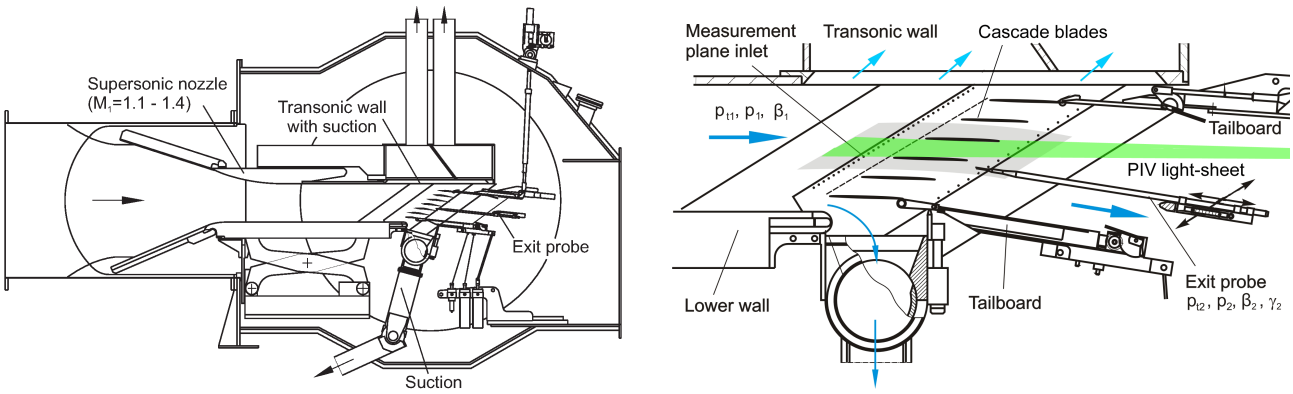

Fig. 1 Left: Schematic of the transonic cascade wind tunnel at the DLR Institute of Propulsion Technology; Right: test section and light sheet orientation for PIV

may impose unsteady downstream conditions to the shock which is a further source of large scale shock oscillations [4].

One way of reducing the size of the separation region above transonic airfoils is to increase the momentum of the boundary layer upstream of the shock by flow control. This can be done by distributed fluid injection which generates streamwise vortical structures that transfers momentum form the outer high speed flow to the boundary layer. Here, so called air jet vortex generators (AJVGs) are applied that consists of a spanwise row of inclined jets that inject fluid coming from the pressure side transverse to the flow direction on the suction side [15]. Another way of making the upstream boundary layer profile fuller and less prone to separation is to trigger the laminar-to-turbulent transition upstream of the SBLI. For the present investigation, this is achieved by increasing the roughness in a span-wise oriented patch placed near the leading edge on the suction side. Separately from investigations on flow control the degree of incoming turbulence is raised significantly to investigate whether this enhances shock motion [4] and possibly blade vibration amplitudes.

The present study provides information about the transient behavior of the SBLI for the aforementioned test cases by classical 2-C PIV with the help of conditional averaging over the shock position using large sets of samples. At the expense of time resolution, as in time-resolved PIV investigations of SBLI [8], this way higher spatial resolutions can be achieved for measurement regions that cover both shock-foot (e.g. lambda-pattern) and the associated separation region. Subsequently, the evaluation of the transition control with regard to reducing the separation region can be carried out by conditional averaging of PIV samples at various positions of the moving passage shock. In addition, the unsteadiness of shock motion will be assessed in terms of a Fourier analysis of the shock position with high spatial and temporal resolution using time-resolved shock shadowgraphs. Furthermore the impact of SBLI control on blade vibration amplitudes and shock motion amplitudes will be evaluated by considering joint probability distributions of both, whereby blade deflections are measured by a correlation based approach in each PIV sample.

2. Test facility and operation conditions

Measurements have been conducted in the transonic cascade wind tunnel of the DLR in Köln (see Fig. 1) at $Ma_1 = 1.21$. The tunnel is a closed loop, continuously running facility. The incoming flow passes through a straight cascade of six airfoils representing a portion of a ring of an actual blade row in an axial compressor or fan. The cascade blades are supported by side walls made of acrylic glass which provide suitable optical access. Boundary layer suction capacities of the facility allow the control of the side wall boundary layer in front of the cascade test section, in the upper

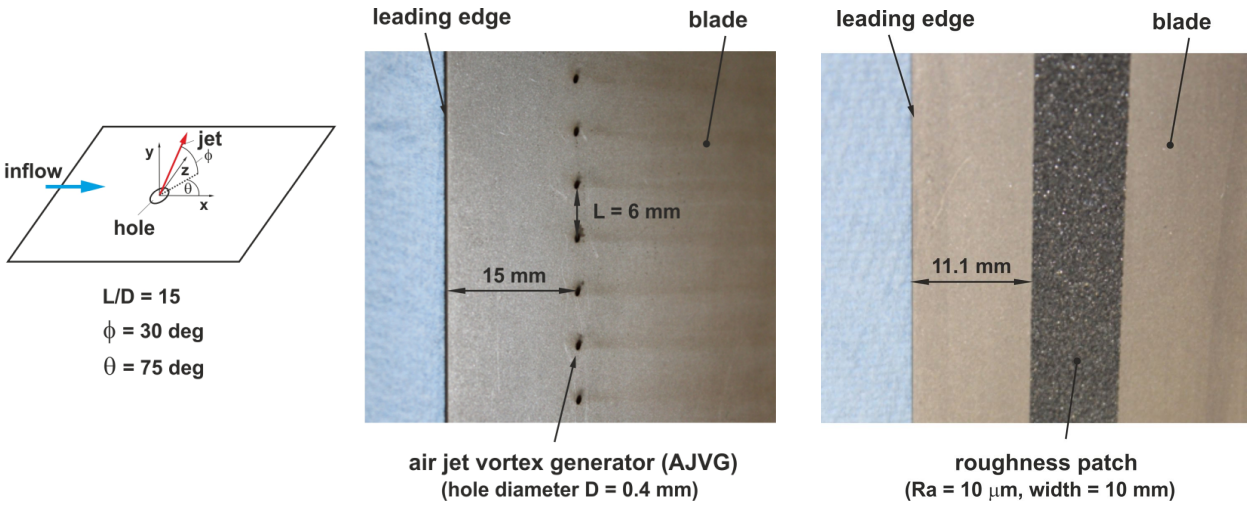

Fig. 2 Left: Schematic diagram of air jet vortex generators (AJVGs); Middle: AJVG arrangement on the suction side; Right: dimensions of the roughness patch on the suction side

and lower bypass channels as well as on the upper and lower end walls. By controlling the latter, a homogeneous inflow representative of an "infinite blade cascade" can be achieved. In addition, suction slots in between the blades provide control of boundary layers on the side walls within the cascade passages to adjust specific axial velocity density ratios at a controlled constriction [9].

The present blade geometry was provided by Rolls-Royce Germany within the EU research project TFAST (Transition Location Effect on Shock Wave Boundary Layer Interaction). The cascade consists of six blades with $c = 100$ mm chord length and 168 mm blade span and exhibits a flow turning of 15° at the aerodynamic design point. For the given inlet Mach number of Ma $= 1.21$ the chord Reynolds number is 1.4×10^6. Static pressure tabs located at mid span of the middle airfoil on both suction and pressure side enable the monitoring of the chord-wise static pressure and isentropic Mach number distributions. Flow conditions are adjusted according to a specific chord-wise Mach number distribution and a constant pitch-wise inflow angle distribution at mid-span for all test cases . The latter was verified by Laser-two-Focus (L2F) measurements [10].

The reference case (laminar case) contains no additional flow conditioning by means of transition control or increase of turbulence. In this case, upstream of the cascade the inflow exhibits a low turbulence intensity (Tu $= 0.5 - 0.8\%$) and laminar-turbulent transition is triggered by the shock boundary layer interaction. For the second case (turbulent case) the turbulence level of the incoming flow is increased by a turbulence grid placed upstream of the test section leading to a turbulence intensity of Tu $= 2.25 - 2.5\%$ in front of the leading edge. The turbulence intensities are verified by hot wire measurements.

Triggering of the laminar-turbulent transition at a fixed location upstream of the shock foot is achieved by patch of increased roughness ($R_a = 10$ μm) of a width of 10 mm that is placed 10 mm downstream of the leading edge on the suction side (see Fig. 2, right). The second configuration applies so called air jet vortex generators (AJVG) that consist of a row of inclined bores of 0.4 mm diameter placed $x = 15$ mm downstream of the leading edge. Through these AJVGs, air coming from the pressure side is blown out in the form of inclined jets issuing into the airstream transverse to the main flow direction at the suction side.

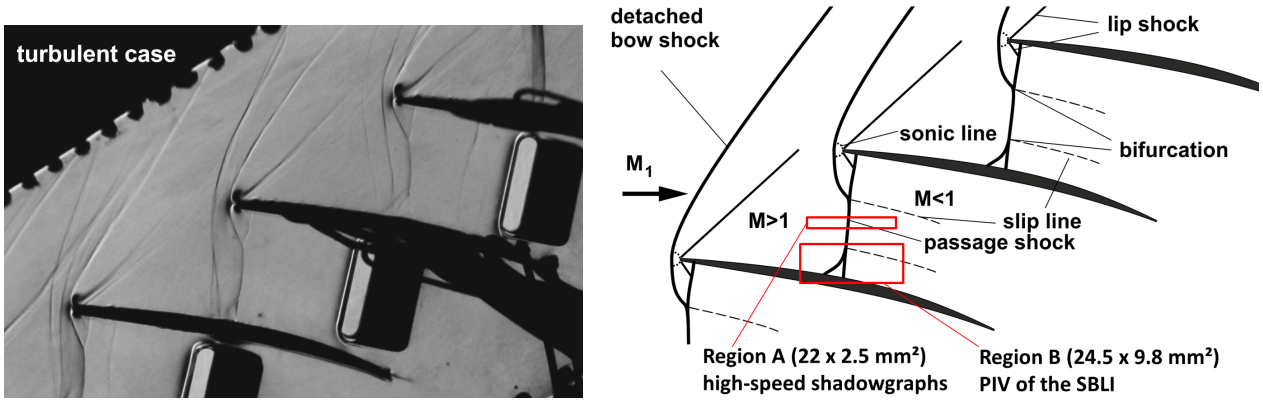

Fig. 3 Schlieren image at turbulent conditions (left) and schematic diagram of the shock system including measurement regions

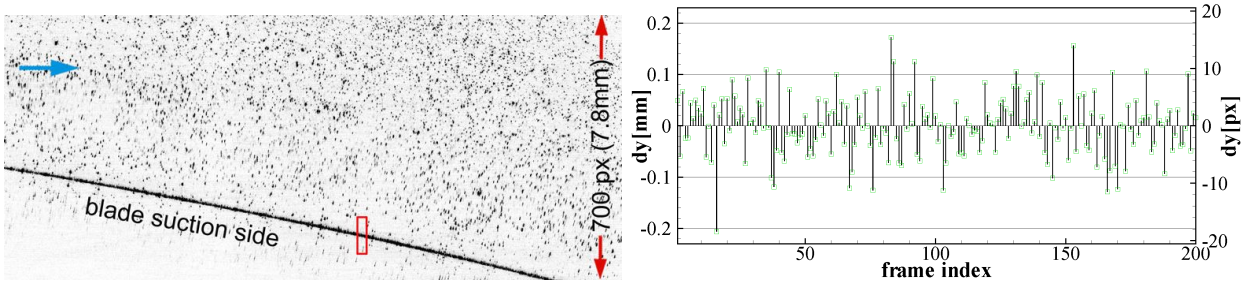

Fig. 4 Left: PIV raw image with rectangular region for evaluation of blade displacements; Right: vertical blade displacements over 200 frames measured within the red rectangular box

3. PIV instrumentation and processing

A planar 2-C PIV setup is applied using a classical normal viewing arrangement with the measurement plane located at midspan. The double-frame camera (laminar case: PCO2000, other: ILA.SCMOS) is equipped with an Nikkor Micro $f = 200$ mm lens at a magnification of M$\approx$ 0.55. PIV measurements of the SBLI have been conducted for a field that covers the shock foot and the separation region near the suction side (region **B** in Fig. 3). Due to restrictions of the optical accessibility the laser light is introduced through a light-sheet probe about 550 mm downstream from the cascade as illustrated in Fig. 1, right. The far downstream distance of the light sheet probe is chosen to minimize disturbances of the flow in upstream direction. More details regarding the light sheet probe and seeding procedure are described in [11].

For measurements of the separation region (region **B**) the tracer density of the conventional paraffin droplet seeding was found to be insufficient and thus a smoke generator is used which generates tracer droplets by evaporation and re-condensation of refined mineral oil leading to droplet sizes below 1 μm. The tracer response to the normal shock has been evaluated from PIV measurements in region **A** ($\Delta t = 0.3$ μs, window size of 0.70×0.70 mm^2). For response time evaluation each single shot velocity profile is fitted against an exponential velocity profile [14, 11]. From this, the characteristic relaxation length of smoke oil tracer deceleration to the 1/e part of the velocity step across the normal shock is estimated with $\xi_p = 0.29 \pm 0.06$ mm and an average relaxation time of $\tau_p = 0.94 \pm 0.18$ μs.

The unsteady aerodynamic loading of the thin blade results in flexure (i.e. vibrations) of up to $\pm$28 pixels ($\pm$0.27 mm). Using a correlation-based algorithm the relative position of the blade surface was determined for each recording and used to offset the image data to a coincident blade position

Table 1 PIV resolutions and accuracies for various test cases

	Magnification [μm/pixel]	Pulse delay Δt [μs]	Field of view ($W \times H$) [mm^2]	Interrogation volume ($W \times H \times D$) [mm^3]	Accuracy[a] [m/s]
Laminar case	11.1	0.4	22.8×7.8	$0.53 \times 0.27 \times 0.5$	2.78
Turbulent case	9.56	0.5	24.4×9.8	$0.46 \times 0.23 \times 0.5$	1.91
AJVG	9.82	0.5	25.1×10.1	$0.47 \times 0.24 \times 0.5$	1.96
Rough. patch	9.92	0.5	25.4×10.2	$0.48 \times 0.24 \times 0.5$	1.98

[a] based on a positional detection accuracy of the signal peak of 0.1 pixel

prior to PIV processing. Therefore, positional blade displacements are evaluated in a small rectangular region above the blade suction side as indicated in Fig. 4, left. Displacements due to camera vibrations are less than 1 pixel which has been scrutinized by recording a fixed point at the tunnel side wall.

PIV image data is processed using PIVScript and PIVview 3.8.0 (PIVTEC GmbH). Isolated low image densities occurred in the separation area. Outlier in these areas were excluded based on a normalized median filter (threshold=6), a dynamic mean test and the signal-to-noise ratio of the signal peak. A vector is rejected if the SNR of the signal peak falls below 5. The PIV resolutions and accuracies achieved are provided in Table 1.

Near the suction side, the shock foot position is fluctuating within a range of up to 23% of chord (23 mm). In order to quantify the mean size of the separation region conditional averaging has been conducted based upon the position of the shock foot in each random PIV snapshot. Therefore in total 10,000 PIV samples are recorded. After PIV processing including compensation of blade vibrations the shock position is estimated through the maximum absolute axial velocity gradient $|\partial u/\partial x|$ across the normal shock wave. Therefore, velocities are averaged over seven top rows of the velocity field in region B (see Fig. 3, right) and differentiation is conducted through a standard least squares approach over five nodes along the x direction [13]. Conditional averaging has been conducted over PIV samples that are sorted after discrete shock positions at a spatial resolution of 1 mm (1% of chord length). If reverse flow becomes visible in the conditionally averaged velocity field, the dividing streamline at zero net mass flux is computed by direct integration of the velocity profile along the y-axis [5].

4. High-speed shadowgraphy setup and processing

In order to analyze the passage shock oscillations with high spatial and temporal resolution time resolved shadowgraphs are recorded using pulsed LED back-illumination [17]. The field of view covers a region of 24×4.42 mm^2 centered with respect to region **A** in Fig. 3. The lens focus lays at midspan. The pulse duration was set to 0.4 μs with a repetition rate of 20 kHz. The high-speed camera (Photron SA-5) is equipped with a Nikkor Micro lens, which is set to a magnification of 35 μm/pixel. More details about the high speed shadowgraphy system can be found in [11]. The shock induced intensity gradients in each shadowgraph are enhanced by background subtraction and image normalization using the average intensity over each image sequence to obtain a homogeneous back-ground intensity. The position of the passage shock x_s is tracked in each image based upon the maximum absolute intensity gradient (see Fig. 5). Occasional erroneous detections due to the finite axial width of the shock shadowgraph were mitigated by a sliding median filter over three samples. The power spectral distribution of shock movement is obtained by a Fourier analysis of the shock position over time using image sequences of up to 127,000 samples. Processing bases on averaging the FFTs of a

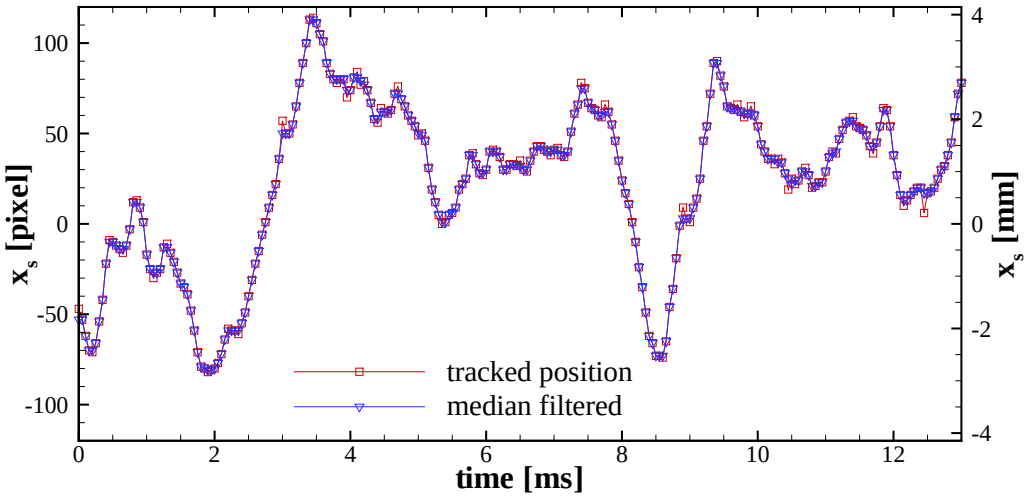

Fig. 5 Position of the passage shock over time in region **A** in Fig. 3 sampled at 20 kHz; Erroneous detections due to the finite axial width of the shock shadowgraph were mitigated by a sliding median filter over three samples

temporally sliding window of a fixed width and overlap [16]. The herein presented data was spectrally analyzed using a sliding window of 2048 samples (102 ms) at 75% overlap. Furthermore the window is weighted by a Hanning-function in order to suppress processing artifacts.

5. Instantaneous PIV results

In every case investigated, the interaction of shock waves and boundary layer is highly unsteady which is exemplary shown in six PIV shots in Fig. 6 recorded for the turbulent test case. Neither the passage shock position nor the extension of the separation region are steady. Regardless of the position of the normal shock wave, different flow states can be identified. Parts of the PIV samples show a weak flow separation together with a normal shock wave with none or only a very weakly pronounced lambda shock system (see Fig. 6, top). Another part of PIV samples exhibits a moderate transonic separation including a lambda shock pattern that consists of a normal shock wave that splits into a an oblique shock and a near normal shock wave (see Fig. 6, middle). Here the oblique shock starts from the point of separation while the near normal shock starts above the separation region. The flow in between is weakly transonic and becomes subsonic downstream of the near normal shock. The reattachment point is located far downstream. In parts of the PIV samples, the subsonic flow downstream of the lambda pattern is separated by a shear layer, that emanates from the point of intersection of the oblique and the normal shock wave (so called "slip line" [3, 1]. Fig. 6, bottom, shows partially occurring strong flow separations involving shape variations of the lambda pattern as well as large vortices occurring downstream of the rear shock.

6. Estimation of the transverse velocity deficit across the slip line

In a few PIV samples, the flow states downstream of the lambda pattern are separated by at slip line (e.g. Fig. 6, middle). To demonstrate the feasibility of estimating the velocity deficit across the slip line from single PIV shots, velocity profiles have been extracted at equidistant x-positions of the measurement presented in Fig. 6, middle, left. These velocity profiles are shown in Fig. 7, wherein the gradient $\partial u/\partial x$ is obtained by a linear fit based on 4-5 grid nodes across the slip line. Within

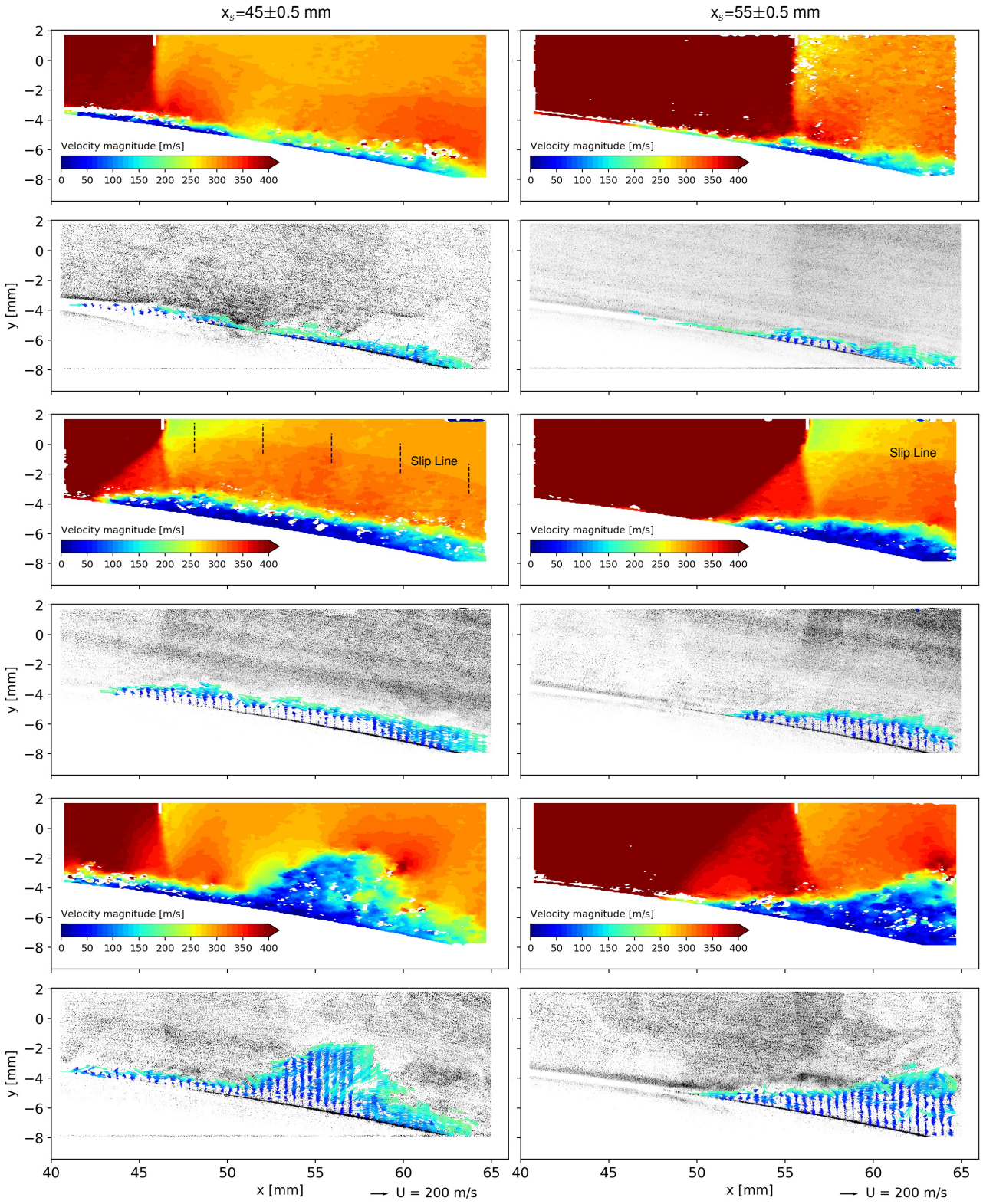

Fig. 6 PIV shots for the turbulent test case with shocks further upstream (left) and downstream (right); vectors at $u > 200$ m/s are clipped; Top: nearly attached flow and normal passage shock; Middle: Flow separation with associated lambda pattern and slip line; Bottom: large flow separation including shape variation of the lambda pattern and occasional reverse flow

a distance to the normal shock between 1.8 mm and 17.4 mm (distance range of 15.6% of chord length) the velocity deficit decreases from 21 m/s down to 9 m/s respectively from 5% down to 2% of u_1. Accordingly, the gradient $\partial u/\partial x$ is more than halved over that distance. The determination of the mean speed deficit at various downstream positions requires the automatic detection of slip line positions in single shots, which is subject of ongoing work.

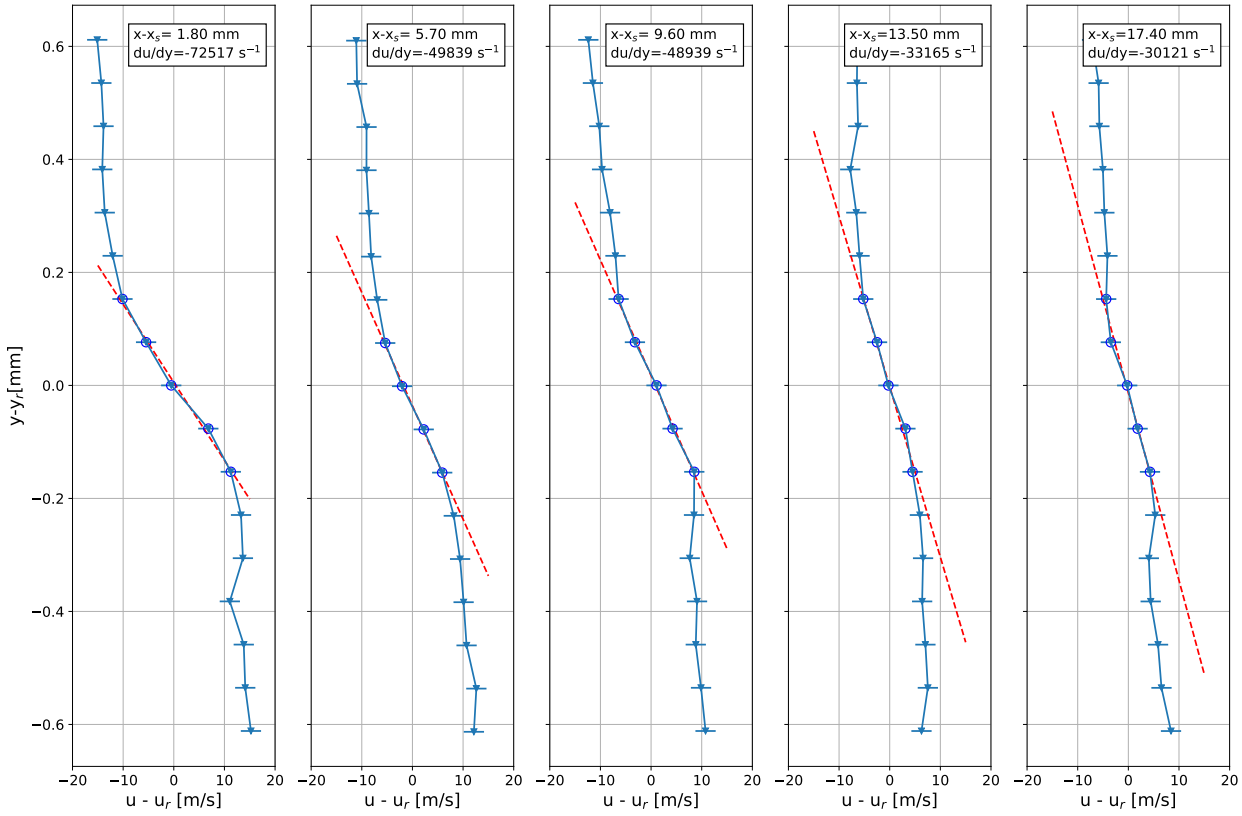

Fig. 7 Instantaneous axial velocities and gradients across the slip line at various stations downstream of the normal shock as marked by vertical dashed lines in Fig. 6, middle, left; Gradients are obtained by a linear fit based on points marked with a circle

7. Size of the separation region and influence on boundary layer thickening

The size of separation region is assessed through conditionally averages PIV samples at various positions of the moving passage shock. The sorting parameter (e.g. estimate of the shock position), is shown in Fig. 6 through a white vertical bar in the upper area of each velocity field.

Velocities fields for all test cases, conditionally averaged at two shock positions of 4 mm spacing are shown in Fig. 8. In case of low turbulence of the incoming flow ($Tu_1 = 0.5\%$) it is assumed that the passage shock interacts with a laminar boundary layer. Massive bubble separation occurs in this case and reverse flow occurs inside the transitional separation bubble (TSB). The chord wise length of the TSB at the rear shock position is about 6 mm longer compared to the TSB length at the frontal shock position. Accordingly, between both shock positions the reattachment point migrates about 6 mm further downstream while the onset of separation remains far upstream. The total length of the TSB is about 17% of chord length at the rear shock position. The increase of the separation length also leads to an increase of displacement thickness downstream of the separation bubble. At the rear shock position, the thickening of the boundary layer leads to a stronger flow acceleration of the

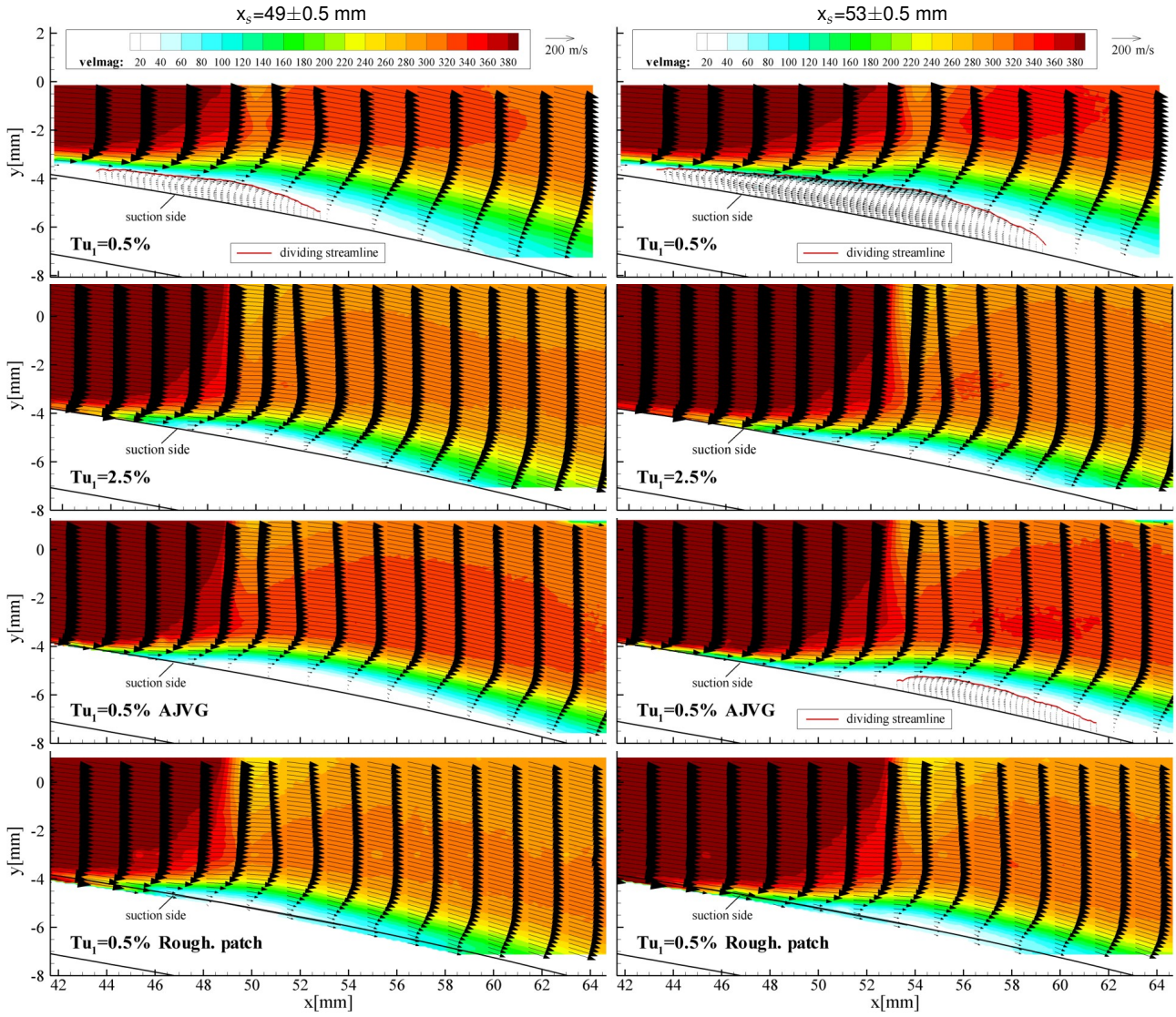

Fig. 8 Mean velocity at shock positions further upstream (left) and downstream (right) by conditional averaging of PIV samples at different shock positions; from top to bottom: laminar test case, turbulent test case, AJVGs and roughness patch

outer flow compared to the outer flow at the frontal shock position. One reason for the fact that the separation bubble becomes larger, the further the shock migrates downstream, could be an increase of the pre-shock Mach number leading to a stronger pressure rise across the shock and thus a stronger adverse pressure gradient.

For the turbulent case (c.f. Fig. 8, second from above), the mean velocity maps at distinct shock positions do not exhibit flow separation although evident from exemplary PIV shots in Fig. 6 (middle and bottom). In this case the shock wave is interacting with a turbulent boundary layer which can stand stronger flow decelerations before separation occurs. Nevertheless, the thickening of the boundary layer is slightly larger for the rear shock position compared to the frontal position.

AJVGs prevent the flow separation in the mean flow at the frontal shock position, but lead to a larger displacement thickness compared to the turbulent case (c.f. Fig. 8, third from above). For the rear shock position, even when AJVGs are used, a separation bubble with reverses flow appears again, but with significantly smaller dimensions compared to the laminar case. In comparison to the laminar

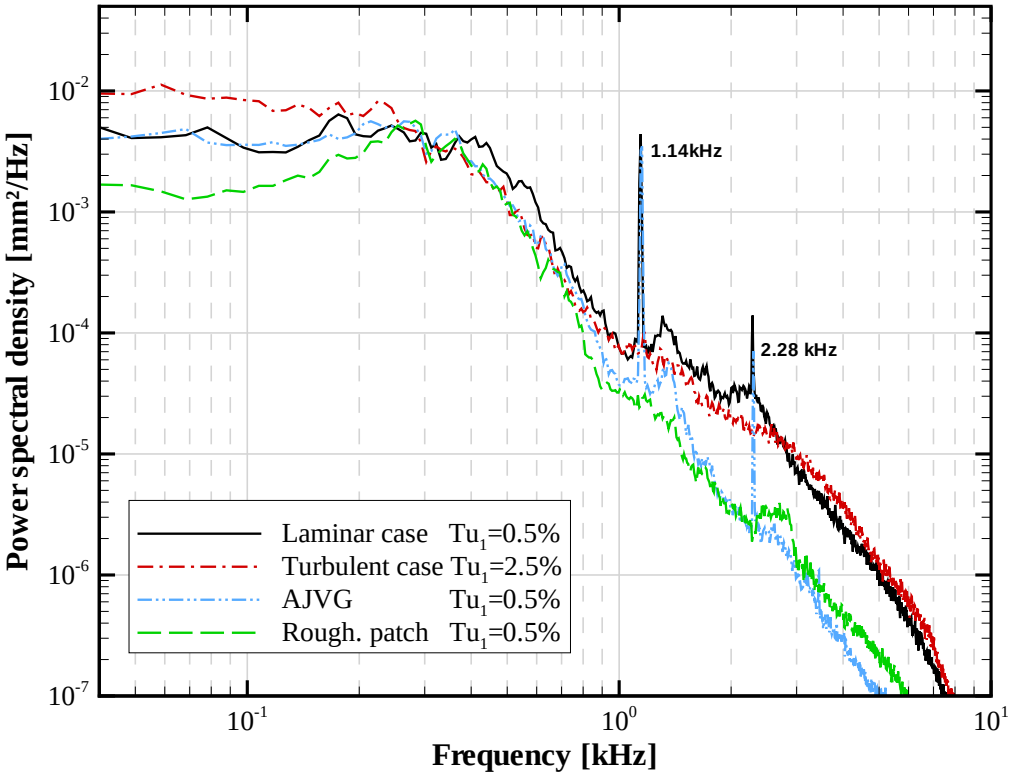

Fig. 9 Power spectral density of passage shock movement obtained from time-resolved shock shadowgraphs recorded in region **A** in Fig. 3

case the starting point of separation is significantly further downstream.

Transition control on the basis of a roughness patch (c.f. Fig. 8, bottom) leads to a significant reduction of the separation region at both the rear and the frontal shock position. The boundary layer thickening downstream of the shock is the lowest for this configuration, which therefore seems to best suited to reduce flow separation under the given operating conditions.

8. Spectral distribution of shock motion amplitudes

Fig. 9 shows the power spectral densities of passage shock motion (i.e. squared amplitudes of shock movement) obtained from high speed shadowgraphs recorded at 20 kHz. For the laminar case and for AJVGs two distinct peaks are noticeable at f=1.14 kHz and at the first harmonic at 2.24 kHz. From literature its is well known that periodic transonic shock oscillations can be triggered either by feedback loops in the separation bubble [4] or by a acoustic wave-propagation feedback from upstream propagating sound pressure waves [12, 7, 6] which source is assumed to originate from vortical flow structures passing over the trailing edge ('trailing edge noise'). Both test cases, which show periodic oscillation (laminar case and AJVGs), also exhibit large variations of bubble separation depending on the shock position (see Fig. 8). Possibly, this bubble separation modulates the boundary layer velocity profile in the vicinity of the shock and/or velocity gradients near the trailing edge which both may support mechanisms that establish a feedback loop.

Apart from isolated peaks, the shock oscillation spectrum is dominated by a broadband spectrum. There are two frequency bands in which the power spectral densities of shock movement differs significantly between the test cases, namely a 'low frequency band' ranging from 0.04 kHz to 0.3 kHz and a 'high frequency band' ranging from 1 kHz to 8 khz. In the low frequency range the highest

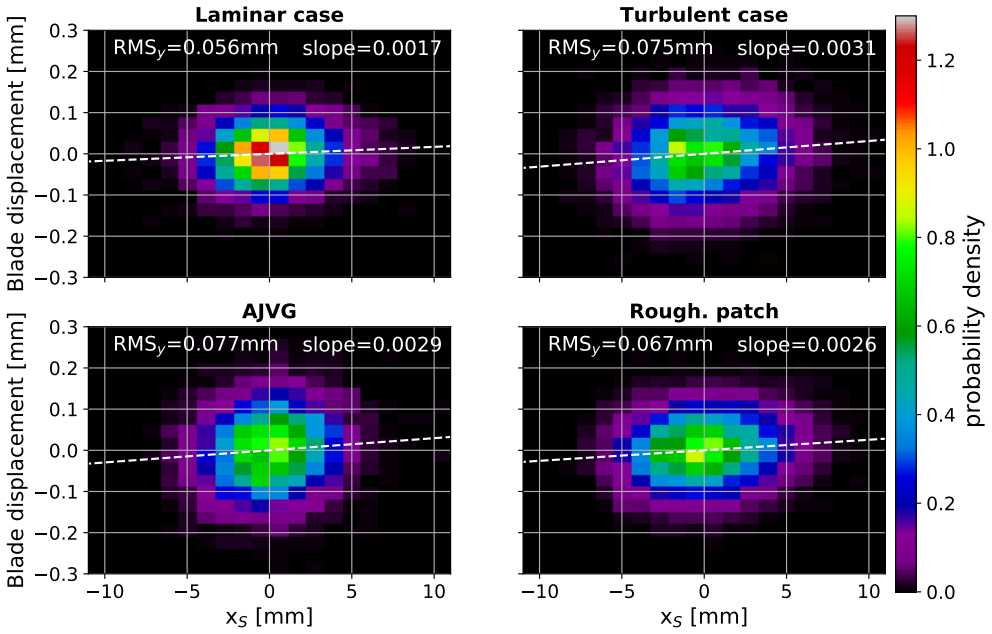

Fig. 10 Joined probability density distributions of transverse blade displacement versus position of the near normal shock in region **B** in Fig. 3

spectral densities occur for the turbulent case. For the laminar case and for AJVGs the spectral densities in the low spectral range (< 0.3 kHz) are very similar and lie between the other two cases. In the high frequency range above 0.7 kHz lower spectral densities are obtained for AJVGs and for the Roughness patch. The case with the least pronounced flow separation (roughness patch) also shows the lowest spectral densities of shock motion.

Increasing the turbulence intensity of the incoming flow is accompanied by larger spectral densities of shock motion although the mean flow exhibits only a weak flow separation (c.f. Fig. 8, second from above).

9. Joined probability density distributions for shock position and positional blade displacements

Where the shock is located on the blade surface influences the integral surface pressure distribution and thus also the lift force that acts on the blade. It is tried to clarify the question whether there is a correlation between the position of the near normal shock and the transverse blade displacement in region **B** (Fig. 3). The latter type of displacement has also been used to correct the blade position in each PIV image.

A linear fit to positional blade displacements as a function of shock position (marked by the dashed line in Fig. 10) indicates a weak dependence of the direction of blade deflection from the shock position for each test case. This is shown in so far as that upward transverse blade displacements are more frequent when the shock is downstream from its mean position while downward transverse blade displacements are more frequent at upstream positions of the shock.

According to Fig. 10 the largest amplitudes of blade displacements occur if AJVGs are applied and for the turbulent case. The latter also exhibits the largest spectral densities of shock motion in the

low frequency range (see Fig. 9). The amplitudes of the blade vibrations are most strongly damped for the laminar case, although strong bubble separation occurs in this case. Also the periodic shock oscillation at f=1.14kHz for the laminar case does not seem to have a strong influence on the vibration amplitudes of the blade. For the remaining cases the RMS of the positional blade displacements is lowest if a roughness patch is applied (RMS=0.067 mm). This coincides with both the lowest spectral densities of shock movement and the most distinctive suppression of flow separation (see Fig. 8).

10. Conclusions

Two passive flow control devices, namely a roughness patch and air jet vortex generators (AJVG), have been compared in regard to their suitability to reduce shock-induced flow separation and shock unsteadiness in a highly loaded compressor cascade at $Ma_1 = 1.21$. In addition, two comparative cascade flows without transition control have been investigated that involve a low and a high degree of upstream turbulence (i.e. 'laminar' and 'turbulent' test case). Exemplary PIV shots indicate strong variations in shape and position of the separation region as well as of the associated lambda shock pattern. Conditional averaging upon different positions of the moving passage shock reveals strong bubble separation for the laminar case while for AJVGs a transitional separation bubble only occurs at rear shock positions. Bubble separation is not evident from conditional averages if a roughness patch is applied for transition control. Also the boundary layer thickening downstream of the shock is less pronounced compared to the turbulent case without transition control.

Separately from PIV, the position of the passage shock has been tracked in time-resolved shadowgraphs at midspan and above the suction side of the central blade of the cascade. From these shadowgraphs the spectral densities (i.e. squared amplitudes of shock movement) have been evaluated by a Fourier analysis. The greatest damping of the shock movement in the low-frequency and high-frequency range is achieved by a roughness patch, in which the separation region is also the least pronounced. Compared to the other cases, the turbulent case contains higher spectral densities in both the low-frequency and high-frequency range. If conditionally averaged PIV results are considered in addition this leads to the conclusion that a reduction of the separation region in size does not necessarily reduce the amplitudes of shock movement.

The jointed probability density distributions of transverse positional blade displacements and amplitudes of shock movement revealed a weak dependency between the position of the near normal shock and the blade deflection. This can be seen in the way that upward transverse blade displacements are more frequent when the shock is downstream from its mean position while downward blade displacements are more frequent at upstream positions of the shock. The dependency is most pronounced for the turbulent test case and for AJVGs, which show the highest amplitudes of the blade vibration compared to the other two test cases. With the exception of the laminar test case, the roughness patch imparted the lowest amplitudes of blade vibrations. It is clear that the blade response to shock oscillations strongly depends on the specific structural and damping characteristic of the airfoil. Further inside could be gained by simultaneous time-resolved recording of shock movement and blade deflection.

References

[1] H. Babinsky and J. K. Harvey, editors. *Shock Wave-Boundary-Layer Interactions*. Cambridge University Press, 2011.

[2] Christopher S. Combs, Phillip A. Kreth, John D. Schmisseur and E. Lara Lash. Image-based analysis of shock-wave/boundary-layer interaction unsteadiness. *AIAA Journal*, 56(3):1288–1293, March 2018.

[3] Jean M. Délery and Reynald S. Bur. The physics of shock wave/boundary layer interaction control: last lessons learned. In *European Congress on Computational Methods in Applied Sciences and Engineering, ECCOMAS, Barcelona*, September 2000.

[4] J.-P. Dussauge and S. Piponniau. Shock/boundary-layer interactions: Possible sources of unsteadiness. *Journal of Fluids and Structures*, 24:1166–1175, 2008.

[5] Edward J. Fitzgerald and Thomas J. Mueller. Measurements in a separation bubble on an airfoil using laser velocimetry. *AIAA Journal*, 28(4):584–592, April 1990.

[6] Nicholas F. Giannelis, Gareth A. Vio and Oleg Levinski. A review of recent developments in the understanding of transonic shock buffet. *Progress in Aerospace Sciences*, 92:39 – 84, 2017.

[7] A. Hartmann, A. Feldhusen and W. Schröder. On the interaction of shock waves and sound waves in transonic buffet flow. *Physics of Fluids*, 25(2):026101, 2013.

[8] Axel Hartmann, Michael Klaas and Wolfgang Schröder. Time-resolved stereo PIV measurements of shock–boundary layer interaction on a supercritical airfoil. *Experiments in Fluids*, 52(3):591–604, 2012.

[9] A. Hergt, S. Grund and W. Steinert. Webpage of the transonic cascade wind tunnel.

[10] A. Hergt, J.Klinner, J. Wellner, C. Willert, S. Grund, W. Steinert and M. Beversdorff. The present challenge of transonic compressor blade design. In *Proceedings of ASME Turbo Expo Oslo, Norway*, number GT2018-75528, June 2018.

[11] J. Klinner, A. Hergt and C. Willert. Experimental investigation of the transonic flow around the leading edge of an eroded fan airfoil. *Experiments in Fluids*, 55(9):1800, 2014.

[12] B.H.K. Lee. Self-sustained shock oscillations on airfoils at transonic speeds. *Progress in Aerospace Sciences*, 37(2):147 – 196, 2001.

[13] M. Raffel, C. Willert, F. Scarano, C.J. Kähler, S. Wereley and J. Kompenhans. *Particle Image Velocimetry*. Experimental Fluid Mechanics. Springer International Publishing AG, 2017.

[14] D. Ragni, F. Schrijer, B.W. van Oudheusden and F. Scarano. Particle tracer response across shocks measured by PIV. *Exp Fluids*, 50(1):53–64, 2011.

[15] F. Tejero, P. Doerffer and O. Szulc. Shock wave induced flow separation control by air-jet and rod vortex generators. *TASK Quarterly : scientific bulletin of Academic Computer Centre in Gdansk*, Vol. 19, No 2:167–180, 2015.

[16] P. Welch. The use of fast Fourier transform for the estimation of power spectra: A method based on time averaging over short, modified periodograms. *IEEE Transactions on Audio and Electroacoustics*, 15(2):70–73, Jun 1967.

[17] C. Willert, D.M. Mitchell and J. Soria. An assessment of high-power light-emitting diodes for high frame rate schlieren imaging. *Exp Fluids*, 53:413–421, 2012.